The water abundance in Jupiter's equatorial zone

23 authors, including:

Andrew Ingersoll
California Institute of Technology
404 PUBLICATIONS   **17,275** CITATIONS

M. A. Janssen
California Institute of Technology
325 PUBLICATIONS   **13,379** CITATIONS

Amadeo Bellotti
Georgia Institute of Technology
13 PUBLICATIONS   **246** CITATIONS

Samuel Gulkis
JPL, California Institute of Technology, Pasadena, CA
337 PUBLICATIONS   **10,796** CITATIONS

Some of the authors of this publication are also working on these related projects:

Project   JUNO Spacecraft View project

Project   Juno Mission View project

The water abundance in Jupiter's equatorial zone

Cheng Li [1*], Andrew Ingersoll [1], Scott Bolton[2], Steven Levin[3], Michael Janssen[3], Sushil Atreya[4], Jonathan Lunine[5], Paul Steffes[6], Shannon Brown[3], Tristan Guillot [7], Michael Allison [8], John Arballo[3], Amadeo Bellotti[9], Virgil Adumitroaie[3], Samuel Gulkis [3], Amoree Hodges[6], Liming Li[10], Sidharth Misra[3], Glenn Orton[3], Fabiano Oyafuso [3], Daniel Santos-Costa[2], Hunter Waite[2] and Zhimeng Zhang[1]

Oxygen is the most common element after hydrogen and helium in Jupiter's atmosphere, and may have been the primary condensable (as water ice) in the protoplanetary disk. Prior to the Juno mission, in situ measurements of Jupiter's water abundance were obtained from the Galileo probe, which dropped into a meteorologically anomalous site. The findings of the Galileo probe were inconclusive because the concentration of water was still increasing when the probe ceased sending data. Here we report on the water abundance in the equatorial region (0 to 4 degrees north latitude), based on data taken at 1.25 to 22 GHz from the Juno microwave radiometer, probing pressures of approximately 0.7 to 30 bar. Because Juno discovered the deep atmosphere to be surprisingly variable as a function of latitude, it remains to confirm whether the equatorial abundance represents Jupiter's global water abundance. The water abundance at the equatorial region is inferred to be $2.5^{+2.2}_{-1.6} \times 10^3$ ppm, or $2.7^{+2.4}_{-1.7}$ times the elemental ratio of protosolar oxygen to hydrogen (1σ uncertainties). If this reflects the global water abundance, the result suggests that the planetesimals that formed Jupiter were unlikely to have been water-rich clathrate hydrates.

From thermodynamic calculations[1], three types of cloud layers in the Jovian atmosphere are thought to exist: an ammonia ice cloud, an ammonium hydrosulfide ice cloud[2,3], and a water ice and droplet cloud, formed approximately at 0.7 bar, 2.2 bar and 5 bar, respectively, assuming solar abundances. The locations of these clouds may vary as a result of the local abundances, meteorology and specific model parameters. Condensation and evaporation of water contribute to weather on giant planets because water is the most abundant species apart from hydrogen and helium and the latent heat flux in convective storms is comparable to the solar and internal heat fluxes[4,5]. Consequently, the thermal state of the atmosphere is affected by the amount of water vapour in the atmosphere. Prior to the Juno mission, in situ measurements of Jupiter's atmospheric composition below the clouds were obtained from the Galileo probe[6], which dropped into a meteorologically anomalous site (6.57° N planetocentric latitude, 4.46° W longitude)[7], known as a 5-μm 'hotspot' near the boundary between the visibly bright equatorial zone (EZ) and the dark north equatorial belt[8]. The findings of the Galileo probe were puzzling because they showed that where ammonia and hydrogen sulfide become uniformly mixed occurs at a level much deeper (~10 bar) than what was predicted by an equilibrium thermochemical model[1]. The concentration of water was subsolar and still increasing at 22 bar, where radio contact with the probe was lost, although the concentrations of nitrogen and sulfur stabilized at ~3 times solar at ~10 bar[9,10]. The depletion of water was proposed to be caused by meteorological effects at the probe location[8,11]. The observed water abundance was assumed not to represent the global mean water abundance on Jupiter, which is an important quantity that distinguishes planetary formation models[12–16] and affects atmospheric thermal structure[17,18]. The Juno mission was in part

motivated by the need to determine the water abundance at multiple locations across the planet. Here we report on the initial analysis of the EZ defined as 0° to +4° latitude, the first of Jupiter's regions to be analysed.

We analysed the first eight of Juno's orbits around Jupiter (designated as PJ1, PJ3, PJ4, PJ5, PJ6, PJ7, PJ8 and PJ9), with each perijove probing a cross-section of Jupiter's atmosphere at a different longitude and spanning latitudes from the north pole to the south pole; no microwave radiometer (MWR) data were obtained during PJ2. Dates and longitudes of each perijove are summarized in Supplementary Table 1. The raw data (antenna temperatures) were processed through a deconvolution algorithm (see Methods and Janssen et al.[19]) that removes synchrotron radiation and microwave cosmic background radiation to recover calibrated atmospheric brightness temperatures whose emission angle dependence is parameterized by three coefficients with spatial resolution constrained by geometry and the antenna beam. The subset of nadir brightness temperatures thus obtained from PJ1 to PJ9 is displayed in Fig. 1. The spatial resolution is highest near the equator (~0.5°) and lowest toward the poles because the spacecraft is closer to the planet near the equator (~4,000 km above the 1 bar level) and further away near the poles. Despite an approximate 45° separation in longitude between each of the PJ1 to PJ9 orbits, the observed nadir brightness temperatures show extremely good consistency, especially at latitudes near the equator, at mid-latitudes, and at pressure levels larger than 10 bar. Compared to the simulated brightness temperatures of a reference adiabatic atmosphere, the observed nadir brightness temperatures are warmer than expected at all channels everywhere except within a narrow latitudinal range of a few degrees located near the equator. This analysis has extended the latitudinal coverage to
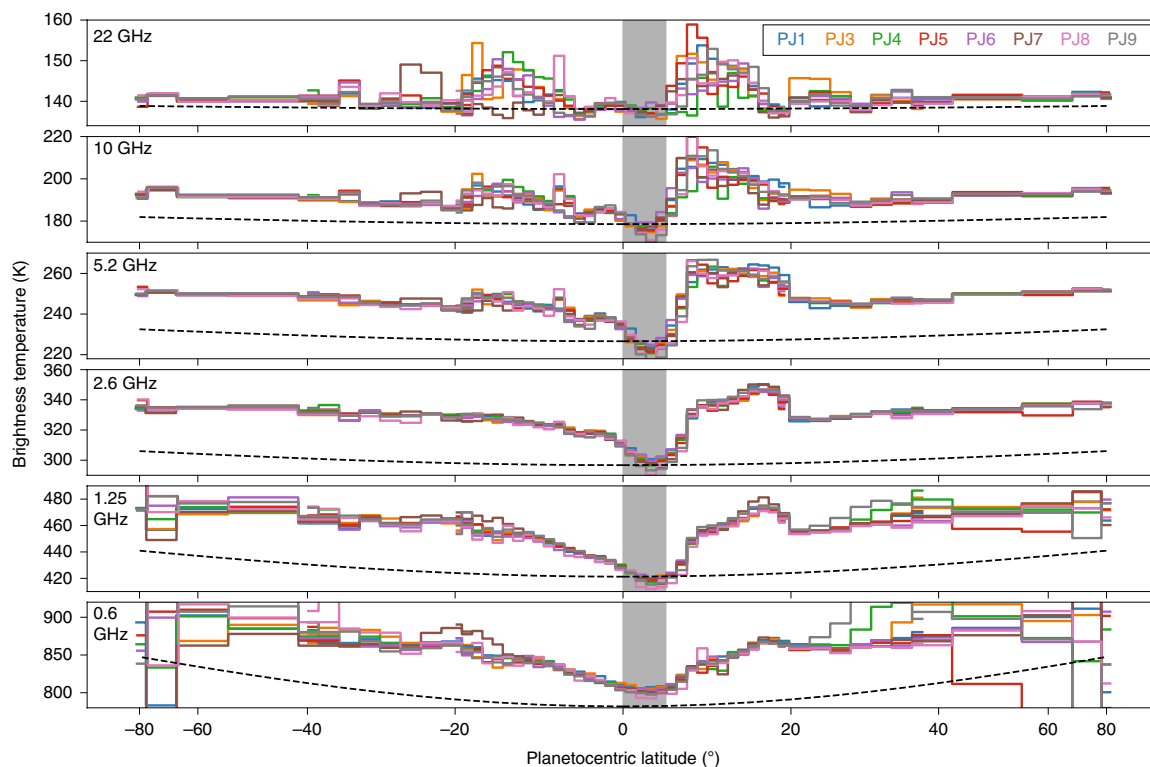
Fig. 1 | Nadir brightness temperatures of perijoves PJ1 to PJ9. The abscissa is planetocentric latitude, scaled by the sine function. Brightness temperatures (the ordinate) of MWR channels at 0.6 GHz–22 GHz are ordered from bottom to top. The perijoves are distinguished by different colours, as indicated. Small step functions in each curve represent the resolution element in latitude, which is hand-tuned using PJ1 data (about 1° from 20° south to 20° north, 2° from 20° to 40° north and south, and 8° from 40° to 90° north and south). Black dashed lines are reference nadir brightness temperatures of an ideal moist adiabatic profile with potential temperature being 132 K referenced at 0.5 bar, and with ammonia and water abundance being 2.7 times solar.

the poles, whereas our previous analysis based on PJ1 data[20] was confined to within 40° of the equator.

Figure 1 shows that the values of the brightness temperature in the EZ are consistent with an ideal moist adiabat in which the temperature is moist adiabatic and the condensing species are well mixed up to their condensation levels. This is also in line with the lack of lightning observations in this region[21] because an ideal moist adiabatic temperature profile does not have enough convective available potential energy to produce lightning. A free inversion of the vertical distribution of ammonia gas using observed nadir PJ1 data[20,22] produced a nearly uniform distribution of ammonia gas, from ~100 bar to 1 bar within a few degrees of the equator, which further corroborates the observation that the ammonia gas in the EZ is mixed vertically to a greater degree than at other latitudes. The consistency between multiple perijoves confirms that the uniformity of ammonia in the EZ is independent of longitude. In addition, similar enrichment of ammonia gas in the EZ relative to the other latitudes was also found by the Cassini/CIRS retrievals[23] and VLA observations[24] although they were sensitive to only shallow levels and pressures less than a few bar. Thus, we identify the EZ as a region that is appropriate for deriving the water abundance, assuming that the temperature profile follows a moist adiabat.

The MWR instrument measures the brightness temperature both at nadir and off-nadir angles. The precision of the angular dependence of the brightness temperature provides important additional information and a tight constraint on atmospheric structure beyond that available from the nadir brightness temperature alone. This is due to the fact that an absolute calibration uncertainty of about 2% does not affect the relative brightness at different angles[19]. We define

the limb-darkening parameter, $R(\theta)$, as the fractional reduction of the brightness temperature when viewing off-nadir:

$$R(\theta) = \frac{T_b(\theta) - T_b(0)}{T_b(0)} \quad (1)$$

where $T_b(\theta)$ is the brightness temperature at emission angle θ. Figure 2 shows the limb-darkening at an emission angle of 45° versus the nadir brightness temperature of all channels. Different colours identify different orbits, from PJ1 to PJ9. Error bars associated with each dot represent 1σ uncertainties due to the deconvolution and the instrument noise. The scattering of dots shows the variability of the atmosphere over longitude and time. It should be noted that three types of orbital attitudes are used. For the MWR and MWR/tilt orbits, the spacecraft is oriented so that the scan circle of the antenna beams always includes the Jupiter nadir. For the gravity orbits, the spacecraft spin axis is oriented toward the Earth, resulting in larger minimum emission angles as the orbit precesses. The consistency of multiple different orbits and the absence of systematic correlation between the nadir brightness temperature and the limb darkening in 0.6–5.2 GHz channels indicate that nadir brightness temperature and limb darkening are two independent measures of the thermal and compositional properties of the atmosphere. Nadir brightness temperature and limb darkening have larger correlations in the 10 GHz and 22 GHz channels because the limb darkening is small in these channels owing to narrower weighting functions and its estimation, by the deconvolution process, is influenced by the nadir brightness temperature.

Even though the EZ region is characterized by a greater degree of mixing, MWR data indicate possible departures from an ideal
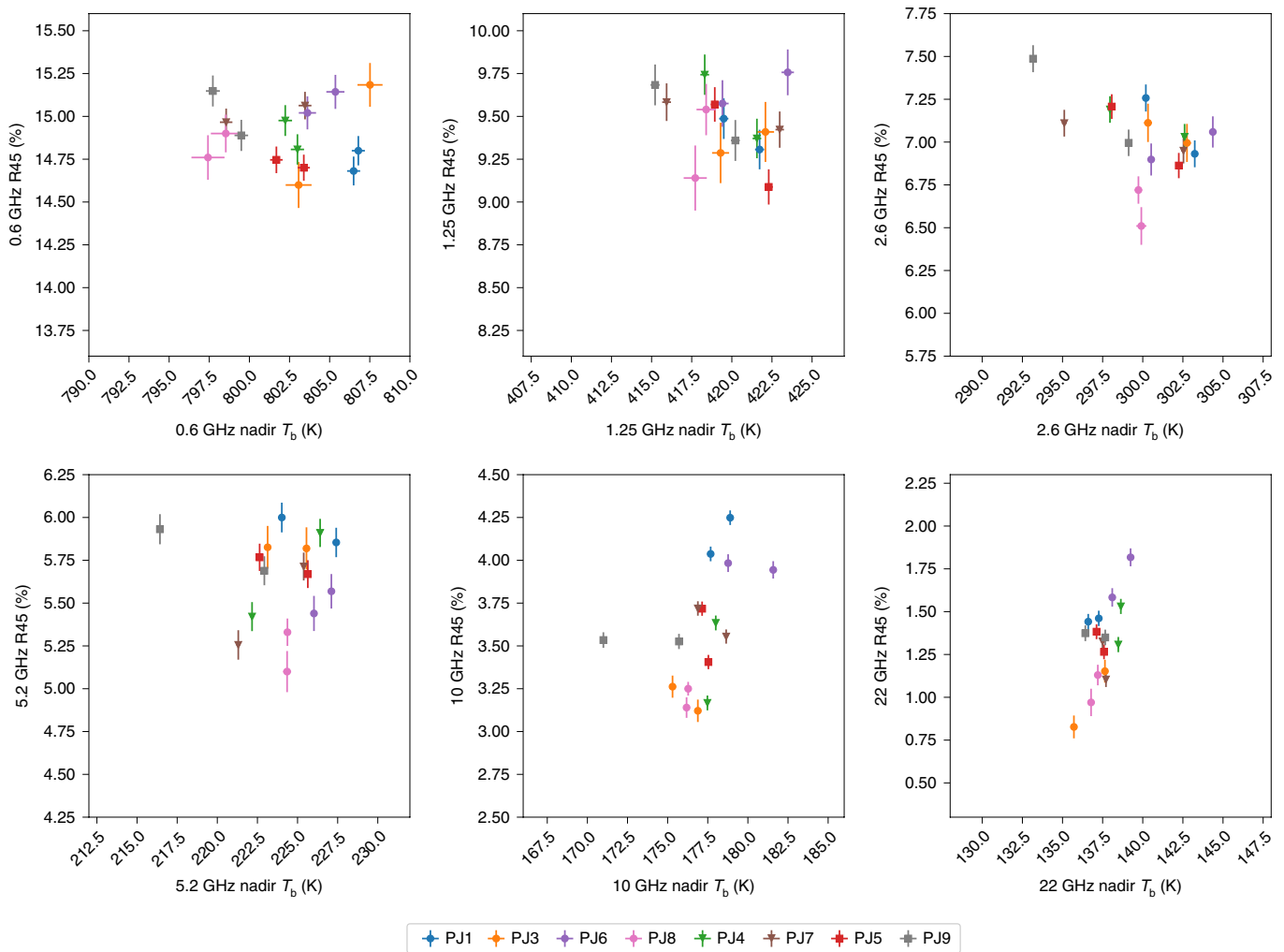
Fig. 2 | Limb darkening versus nadir brightness temperature for each channel in the north EZ (0°–4° N). The vertical axis of each panel spans 2% in limb darkening evaluated at 45° emission angle. Each perijove has two data points. One is averaged between 0–2° N and the other is averaged between 2–4° N. The colour for each perijove is the same as that in Fig. 1. PJ1, PJ3, PJ6 and PJ8 are gravity orbits, indicated by circles. PJ4 and PJ7 are MWR orbits, indicated by triangles. PJ5 and PJ9 are MWR tilt orbits, indicated by squares. The error bar of each data point represents the estimated error, taking into account instrument noise and the deconvolution of antenna beams.

moist adiabat. MWR observations at the 5.2 GHz and 10 GHz channels (Fig. 1) measure slightly colder brightness temperatures (by ~5 K) than the ideal moist adiabatic model. The potential change in temperature due to ammonia condensation/vaporization at these levels is only $x\mathrm{NH_3} L_{\mathrm{NH_3}}/c_{P,\mathrm{H_2}} \approx 0.3\,\mathrm{K}$—where $x\mathrm{NH_3}$ is the ammonia mole fraction, $L_{\mathrm{NH_3}}$ $L\mathrm{NH_3}$ is the latent heat of ammonia, and $c_{P,\mathrm{H_2}}$ is the specific heat of $\mathrm{H_2}$ at constant pressure—and therefore does not account for the observations. To account for the coldness, we allow the possibility that ammonia abundance is enriched by 10–15% (parameterized by the factor f_x in equation (3) with respect to the deep abundance near a pressure of a few bar). Simulation of two-dimensional moist convection in Jovian atmospheres[25] suggests that the slight enrichment of ammonia in the sub-cloud layer is made possible by evaporated ammonia precipitation. The cold plumes of ammonia-rich precipitation sink into the atmosphere to a pressure of a few bar, where they encounter stable layers caused by an increase in the water abundance. This creates a local maximum in ammonia concentration—referred to as the enriched ammonia layer—that is consistent with the observations. As a result, the model for the ammonia distribution consists of five parameters: (1) the ammonia enrichment factor f_x, (2) the pressure of the enriched

ammonia layer p_D, (3) its thickness Δp, (4) the deep ammonia abundance $x\mathrm{NH_3}$ and (5) the deep water abundance $x\mathrm{H_2O}$. Since we do not know the functional form of the ammonia profile $q(p)$ in the enriched ammonia layer, we use an exponential profile that results from balancing the downward diffusive flux and upward advective flux. Its functional form in pressure coordinates is:

$$q(p) = A + B \exp\left(-\frac{p - p_\mathrm{D}}{\Delta p}\right) \tag{2}$$

where p is pressure, p_D is the pressure level that the stable layer starts to develop, $p > p_\mathrm{D}$, and Δp is its thickness in pressure. Two constants A and B are determined by matching the boundary conditions:

$$
\begin{aligned}
q(p) &= x\mathrm{NH_3}, \quad p \to \infty \\
q(p) &= f_x \cdot x\mathrm{NH_3}, \quad p \leq p_\mathrm{D}
\end{aligned}
\tag{3}
$$

which imply that the ammonia abundance is enriched by a factor of f_x with respect to the deep abundance at pressure levels less than p_D. The resulting ammonia profile is displayed in Fig. 4d, where a small kink in the ammonia profile is visible.
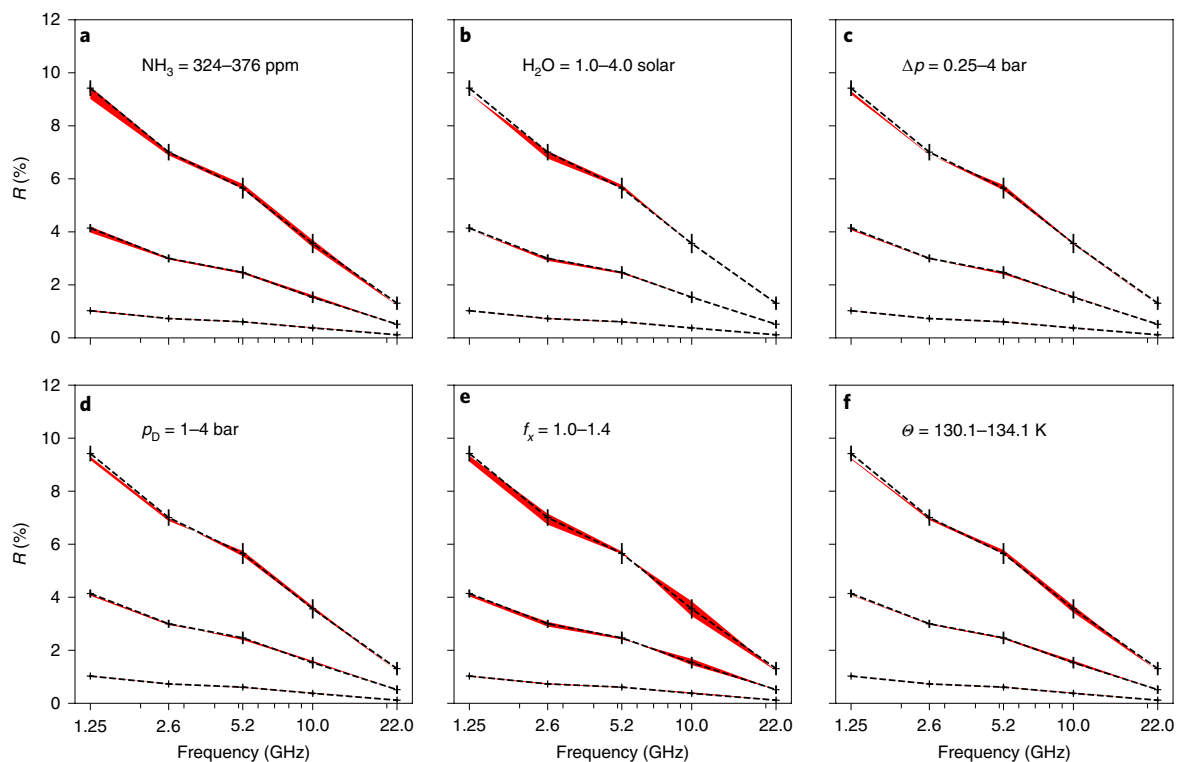
Fig. 3 | Sensitivity study of model parameters. The reference profile is constructed by the state vector $X = (350\ \text{ppm}, 2.0\ \text{solar}, 1\ \text{bar}, 2\ \text{bar}, 1.2\ \text{K}, 132.1\ \text{K})$. Three black lines in each panel show the limb darkening at 45°, 30° and 15° emission angles, respectively, from top to bottom. The red-shaded area shows the range of the limb darkening when each parameter is varied within the values indicated. The vertical error bars roughly represent limb-darkening uncertainties at 2σ level.

We first examine qualitatively the sensitivity of limb darkening to these parameters by varying each parameter while holding the others constant. The results are in Fig. 3. The objective is to identify which parameter is constrained by which channel. Our reference state, based on fitting the nadir-only MWR measurements, is $x\text{NH}_3 = 2.7$ times solar, $x\text{H}_2\text{O} = 2.0$ times solar, $\Delta p = 1$ bar, $p_D = 2$ bar, $f_x = 1.2$ and potential temperature $\Theta = 132\ \text{K}$ (referenced to $0.5\ \text{bar}$)[26]. From this reference state, $x\text{NH}_3$ is varied from 2.5 to 2.8 times solar, equivalent to 324 ppm to 376 ppm (Fig. 3a); $x\text{H}_2\text{O}$ is varied from 1.0 to 4.0 times solar (Fig. 3b); Δp is varied from 0.25 to 4.0 bar (Fig. 3c); p_D is varied from 1 to 4 bar (Fig. 3d); f_x is varied from 1.0 to 1.4 (Fig. 3e); and Θ is varied from 130.1 K to 134.1 K (Fig. 3f). Three spectra of the limb-darkening, evaluated at 45°, 30° and 15°, are plotted against frequency in gigahertz. Since the width of the shaded area is proportional to the sensitivity of the parameter studied, Fig. 3c,d,f show that the limb darkening is not sensitive to the choices of p_D, Δp and Θ. Therefore, the precise location, thickness and functional form of the ammonia-variable layer do not affect our retrieved deep ammonia abundance. For example, one may use a linear interpolation for the ammonia profile that starts at pressure level p_D and ends at pressure level $(p_D, -\Delta p)$; this does not change our result. Figure 3a shows that the 1.25-GHz channel is most sensitive to the deep ammonia abundance. As demonstrated in Fig. 3b and in Janssen et al.[19], the 2.6-GHz channel exhibits the most sensitivity to the water abundance because the limb-darkening value is largest when the water abundance changes significantly, which is at the water condensation level. Since the limb darkening of this channel is also affected by f_x (Fig. 3e), there is a potential correlation between the estimation of the water abundance and the ammonia enrichment factor, a reason why f_x must be included in the forward model to allow a conservative estimate of the water abundance. But because the 10 GHz channel is more sensitive to f_x than the other

channels, it can be used to determine f_x, while the 2.6 GHz channel determines $x\text{H}_2\text{O}$ and the 1.25 GHz channel determines $x\text{NH}_3$.

We then use a Markov Chain Monte Carlo sampler to assess the posterior probability distribution of the parameters based on the average of all perijoves in the current study observed at the 1.25 GHz (24 cm), 2.6 GHz (11.5 cm), 5.2 GHz (5.8 cm), 10 GHz (3 cm), and 22 GHz (1.4 cm) channels (see Methods). Brightness temperatures from the 0.6 GHz channel (50 cm) are not part of this analysis because the opacity of ammonia and water are not known well enough at the greater pressure and temperatures probed with this frequency[27]. In Supplementary Information A we provide a simulation of results for the EZ using the 0.6 GHz channel assuming its opacity is well known, and we obtain a substantial improvement to our precision. The simulation shows that further laboratory data would be useful to constrain the water abundance beyond 30 bar. All mixing ratios in this article refer to molar mixing ratios and the solar photospheric abundances are according to table 1 of Asplund et al.[28], adjusted to protosolar values[29]. They are also summarized in Supplementary Table 2.

A sample of thermal and compositional profiles explored by the sampler is displayed in Fig. 4, with the median profiles marked in black. The final statistics are expressed by the symbol $A_{-\delta}^{+\sigma}$, where $A - \delta$, A and $A + \sigma$ represent the 16th, 50th and 84th percentiles of the samples (1σ uncertainty) in the marginal distribution. The values are relevant for pressures less than about 30 bar where the contribution function of the 1.2-GHz channel peaks. Figure 5 shows the marginal probability density functions of the ammonia abundance, the water abundance and the ammonia enrichment factor. The distribution of p_D and Δp (not shown) are flat, as expected from the sensitivity study; Θ is distributed similarly to the prior, implying that the observation does not contain more information about Θ than the prior (not shown).
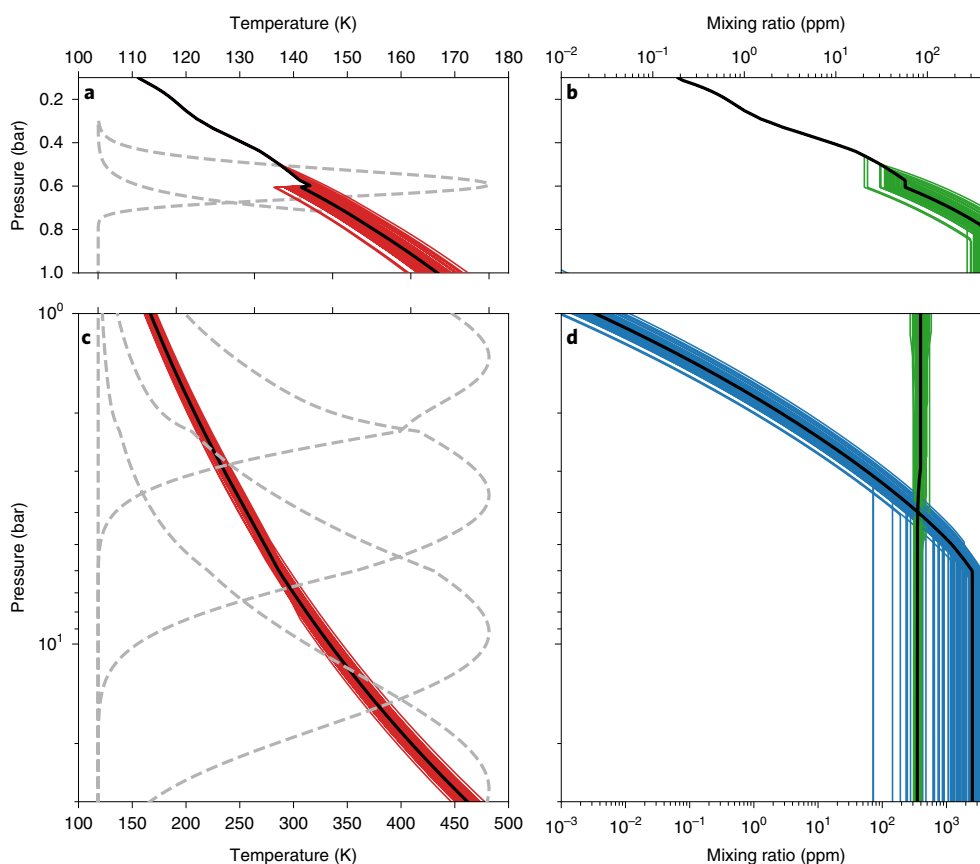
Fig. 4 | Sample of thermal and compositional profiles explored by the Markov Chain Monte Carlo sampler. a, Temperature profile above the 1-bar pressure level and normalized contribution functions of the 22-GHz channel and the 10-GHz channel. **b**, Ammonia profile above the 1-bar pressure level. **c**, Temperature profile from 30 bar to 1 bar and normalized contribution functions of 10 GHz, 5.2 GHz, 2.6 GHz and 1.2 GHz from top to bottom. **d**, Ammonia and water profile from 30 bar to 1 bar. The black lines indicate the median atmospheric model in all samples. The coloured lines (red for temperature, blue for water and green for ammonia) show 100 random samples drawn from the whole probability distribution. The profiles above ~0.6 bar are replaced with the CIRS observations[38], which sometimes leads to a discontinuity at this pressure level.
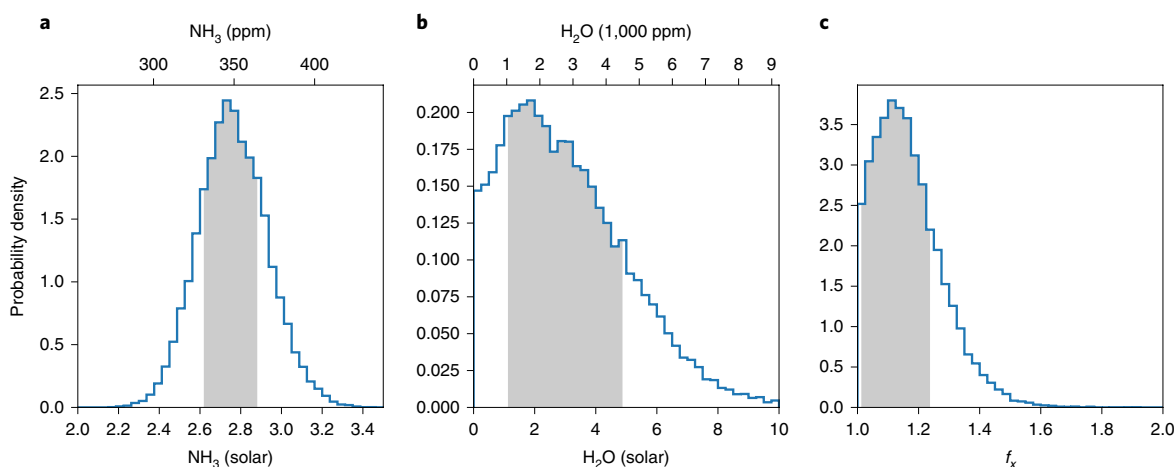

Fig. 5 | Marginal probability density functions of the ammonia abundance, the water abundance and the ammonia enrichment factor. Probability density functions of ammonia (**a**), water (**b**) and ammonia enrichment factor (**c**) estimated by a Markov Chain Monte Carlo sampler using the MWR data from latitudes 0–4° N. The shaded area marks the 1σ confidence interval (16th to 84th percentile). A study using synthetic data is provided in Supplementary Fig. A2 for comparison.

The overall estimate of the ammonia abundance is 351^{+22}_{-21} ppm, or $2.76^{+0.17}_{-0.16}$ times solar, which is consistent within errors with our previous result, 362^{+33}_{-33} ppm (ref. [20]). Although the location of this estimate is not directly comparable to the location of the Galileo measurement, our estimate is at the lower limit of the Galileo Probe Mass Spectrometer's (GPMS) range (566 ± 216 ppm)[10] and is about
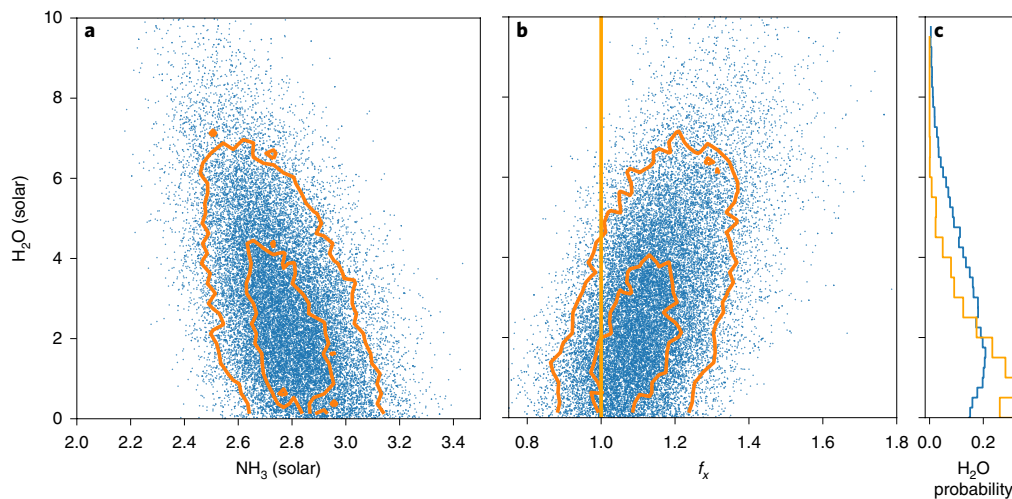
Fig. 6 | Correlation between water, ammonia and the ammonia enrichment factor. Correlation between the water abundance and the ammonia abundance (**a**) and the ammonia enrichment factor (f_x) and the water abundance (**b**). Each dot represents one state in the Markov chain. The density of the dots is proportional to the probability. Two contours show 1σ and 2σ confidence intervals. Panel **c** shows the overall marginal probability distribution for the water abundance (blue line) and the marginal probability distribution for the water abundance assuming $f_x = 1$ (orange line). The blue line is the same as that in Fig. 5b.

a factor of two smaller than that suggested by the radio attenuation of the signal from the Galileo Probe (700 ± 100 ppm)[30]. We speculate that the discrepancy may be an overestimation of the radio attenuation due to signal loss by scintillation of the coherent signal caused by atmospheric turbulence. We note that the values used in the ground-based VLA observations (570 ppm and 400 ppm)[24,31] cannot provide an independent estimate of the deep ammonia abundance owing to confusion from synchrotron radiation in the foreground at long wavelengths. Rather, the Galileo values are used as the prior lower boundary condition and the ammonia abundance is adjusted for the pressure range within which the VLA data can be confidently interpreted. Our analysis utilizes the limb-darkening observations unique to the Juno mission and is an original estimation independent of the previous ones.

The overall water abundance is $2.5^{+2.2}_{-1.6} \times 10^3$ ppm, or $2.7^{+2.4}_{-1.7}$ times solar, with a long tail towards the larger values. The estimated ammonia and water abundance are negatively correlated because increasing either the ammonia abundance or the water abundance will reduce both the nadir brightness temperature and the limb darkening (Fig. 6a). Ranges of water abundances as a function of ammonia abundance are summarized in Table 1. Although the centroid of the abundance values for water and ammonia expressed in terms of solar abundance lie on top of each other, we caution that both the magnitude of the error bars and their symmetry differ for the two determinations. In the case of ammonia, the error bars are small and symmetric; in the case of water, our error bars are larger with a tail towards higher values. The potential range of the enrichment ratios for water versus ammonia allows for water to be less enriched than ammonia (solar versus 2.6 times solar) or much more enriched (5 times solar versus 2.9 times solar). Moreover, the quoted uncertainty range encompasses the 16th to 84th percentile of the probability space. A 2σ (2.5th to 97.5th percentile) uncertainty of the water abundance is $2.7^{+4.8}_{-2.6}$ times solar. Until we are able to utilize the 0.6-GHz channel data, we cannot definitively rule out zero water from fitting the MWR spectra. However, a lower limit of the deep water abundance can be inferred by other evidence such as the existence of lightning[21] or infrared observations. For example, Bjoraker et al. measured an unexplained cloud opacity at 5 bar in the Great Red Spot, which may indicate a minimum water abundance of 1.1 times solar at shallow depths[32]. In addition, multiple authors[18,33,34] have pointed out that beyond a water molar mixing ratio threshold

Table 1 | Ranges of water abundances as a function of ammonia abundance

Ammonia (protosolar)	Ammonia (ppm)	Water (protosolar)	Water (1,000 ppm)
2.6	330	$4.1^{+2.1}_{-2.1}$	$3.8^{+1.9}_{-1.9}$
2.8	356	$2.4^{+2.0}_{-1.5}$	$2.2^{+1.9}_{-1.4}$
3.0	381	$1.6^{+1.4}_{-1.0}$	$1.5^{+1.3}_{-0.9}$
$2.76^{+0.17}_{-0.16}$	351^{+22}_{-21}	$2.7^{+2.4}_{-1.7}$	$2.5^{+2.2}_{-1.6}$

The first three rows show the conditional distribution of the water abundance given the ammonia abundance. The last row shows the overall distribution of ammonia and water. The protosolar values are from Atreya et al.[29] and summarized in Supplementary Table 1. These results are based on data at 1.25 GHz to 22 GHz from Juno MWR probing pressures of approximately 0.7 to 30 bar.

of about 9×10^3 ppm, there can be an inhibition of convection and a steep temperature increase at the water condensation level. We have confirmed that the convective inhibition condition does not apply on Jupiter and the moist adiabatic assumption is valid.

Our model successfully reproduces the average MWR measurements of PJ1 to PJ9, both in brightness temperature and limb darkening. The spatial and temporal variability of different perijoves are treated as the ensemble uncertainty shown in Fig. 7 because we have not accounted for the atmospheric variation. As further discussed in Supplementary Information B, our best-fit model is within one standard deviation of all these constraints. Our solutions for all measurements between latitude 0 and 4° N show no correlation between the residual brightness temperature and the emission angle, implying that there is no obvious missing physical ingredient needed. The ammonia enrichment factor f_x is approximately distributed between 1.0 and 1.2 with a sharp cut off for values greater than 1.4. Although the inversion result cannot statistically rule out the possibility of $f_x = 1$ (in terms of 2σ errors), including this parameter provides a conservative estimate of the uncertainty of the inferred water abundance. The degeneracy between f_x and the water abundance is shown in Fig. 6b. f_x is positively correlated with the water abundance because a larger f_x leads to more limb darkening at the 2.6 GHz channel and so does a smaller water abundance. Since no previous studies have indicated the existence of such a region, our estimation of the water
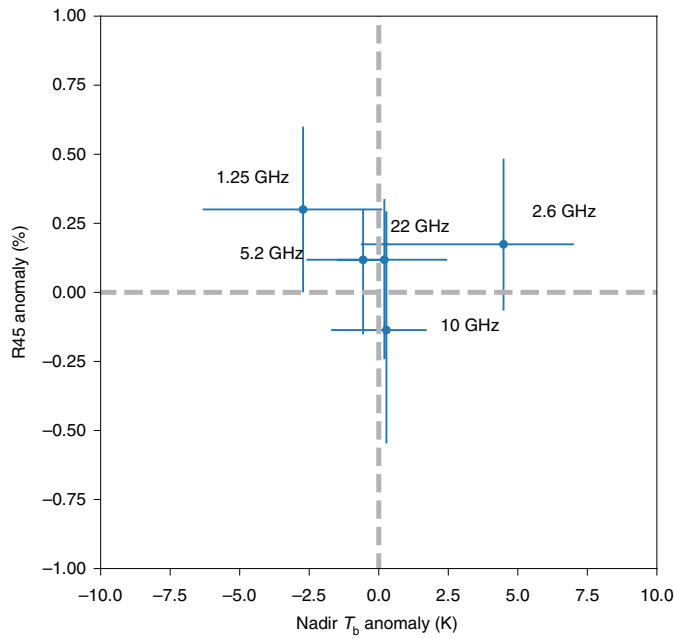
Fig. 7 | Measured brightness temperature and limb-darkening with respect to the best-fitted model. Measured brightness temperature and limb-darkening anomalies for the 1.25–22 GHz channels with respect to the best-fitted model obtained from Juno measurements in the north EZ (0°–5° N). The error bars represent overall uncertainty estimates including atmospheric variability, deconvolution, instrument noise and instrument calibration.

abundance is $1.7^{+1.6}_{-1.2}$ times solar given $f_x = 1$, and the corresponding probability density function is shown in Fig. 6c.

Historically, there has been a strong interest in determining Jupiter's global elemental abundances to aid in our understanding of formation theories of Jupiter and the Solar System. If the value in the EZ is the global value, then (1) at the 1σ level our result is inconsistent with any model of the planetesimal enrichment of Jupiter's envelope that postulates the Galileo probe depletion of O relative to solar to be a global depletion. For example, Lodders et al. constructed a model in which Jupiter's envelope is fed by planetesimals greatly depleted in water and enriched in carbon, so that the total oxygen abundance is only 0.47 times solar[35]. (2) Conversely, planetesimal models in which the trapping of volatiles in a clathrate hydrate from a solar composition disk produces water enrichments 10 times solar[14], supported by observation of the atmospheric waves generated by the Shoemaker-Levy 9 impacts[36], are ruled out. However, a number of other published models produce water enrichments consistent with those derived here, including the trapping of volatiles in cold amorphous ice, leading to an enrichment of O consistent with that of the other major elements and heavy noble gases[12,13] and roughly three times solar O abundance yielded by the equatorial wave analysis[37]. Because our water abundance pertains to the equator only, we shall postpone a thorough discussion of the previous models.

We have shown that the structure of Jupiter's EZ is steady, relatively uniform vertically and close to a moist adiabat; from this we have derived its water abundance. The thermal structure outside of the equator is still ambiguous owing to the non-uniform distribution of ammonia gas, for which we do not know the physical origin. Deriving the thermal structure outside of the equator in the future not only hints about the water abundance on Jupiter at other latitudes but also places constraints on the atmospheric circulation model for giant planets in the Solar System and beyond.

Methods

Deconvolution methods. The brightness temperature at microwave channel λ, latitude ϕ, and emission angle $\mu = \cos(\theta)$ is parameterized by a quadratic representation of the form

$$T_\lambda(\phi, \mu) = \xi_\lambda(\mu)\big(a_\lambda(\phi) + b_\lambda(\phi)(1 - \mu) + c_\lambda(\phi)(1 - \mu)^2\big) \quad (4)$$

where $\xi_\lambda(\mu)$, different for each channel λ, is given by the ratio of the brightness temperature of a model atmosphere and a fit to that model atmosphere only over emission angles less than 53° ($\mu < 0.6$). This ratio equals to one for angles less than 53° but deviates from unity at larger angles. The idea is to fit small angles with a quadratic function but to assume some profile for large angles, which contribute only a small fraction to the antenna temperatures included in the measurement set. For this work, only emission angles less than 45° are used. Therefore, the prefactor $\xi_\lambda(\mu)$ is omitted in the main text.

The performance of the fit was evaluated using an equilibrium cloud condensation model[19], and it was found that the fits were not strongly dependent on the specific model atmosphere chosen to determine $\xi_\lambda(\mu)$. It was found that a quadratic fit of the form given above ($T_B^{(\text{fit})}$) was sufficient to fit the limb-darkening at 45° (evaluated using a real radiative transfer programme, $T_B^{(\text{model})}$) for 1.25–22 GHz channels to within an absolute error of 0.1% (Extended Data Fig. 1) and the nadir brightness temperature to within a relative value of 0.1% (Extended Data Fig. 2) over all perijoves up to PJ9 and over a range of model atmospheres assuming both dry and moist adiabats for all latitudes and spanning ammonia abundances of 2.1 to 3.3 times solar, water abundances of 0.5 to 8 times solar, and half-bar reference temperatures of 130 K to 135.6 K. The maximum errors for 0.6 GHz channel, not included in this analysis, were about twice as large. More details of the deconvolution algorithm, including the treatment of the synchrotron radiation will be summarized in a separate paper.

The measured antenna temperatures are a convolution of the antenna pattern for each channel with brightness temperatures that depend on both emission angle and spatial location. To determine the brightness temperatures a deconvolution must be performed to negate the blurring induced by the instrument antenna pattern. Because the convolution is a linear operation, the set of measured antenna temperatures, T_a, can be represented as the product of a linear operator M with a set of coefficients, X, where the components of X represent information regarding the angular dependence of the brightness temperature at different locations on Jupiter (the $a_\lambda(\phi)$, $b_\lambda(\phi)$, $c_\lambda(\phi)$ coefficients in equation (4)). Then we want to find the optimal solution X^* that minimizes the cost function:

$$(T_a - MX)^T S_a^{-1}(T_a - MX) + (X - X_p)S_p^{-1}(X - X_p) \quad (5)$$

which is:

$$X^* = X_p + \left(M^T S_a^{-1} M + S_p^{-1}\right)^{-1}\left(M^T S_a^{-1}(T_a - MX_p)\right) \quad (6)$$

where X_p is an assumed prior, S_a is the measurement covariance matrix, S_p is a prior covariance, and T_a is the set of measured antenna temperatures, modified to estimate the contribution from synchrotron radiation. The covariance of X^* is a sparse matrix whose sparsity pattern is shown in Extended Data Fig. 3 for the 10 GHz channel. The other channels are similar. The deconvolution process is performed in two steps. First, a coarse grid of 1.2° spacing over the latitude range presented in this work for a and 2.4° for b and c is used without any prior estimate X_p. This step is often sufficient to yield residuals that are within a small multiple of the instrument noise level. The coarse grid solution can then be used as prior estimate for a refined solution on a finer grid to reduce the χ^2 to a value close to 1.

Spectral inversion methods. Let the parameter vector $Z = (x\mathrm{NH}_3, x\mathrm{H}_2\mathrm{O}, f_x, \Delta p, p_D, \Theta)^T$ and the measurement vector $Y = (a_1, b_1, c_1, a_2, b_2, c_2 \ldots, a_5, b_5, c_5)^T$, where a, b and c are the brightness temperature coefficients introduced in equation (4) and their subscripts are channel numbers. We accounted for the limb-darkening via the use of these coefficients. The sensitivity study in the previous section has demonstrated that the 2.6-GHz channel best constrains the water abundance, which is the main objective of this article. We use a Markov Chain Monte Carlo sampler[39] to assess the joint probability of the parameter Z given the observation Y. Bayes' theorem states that:

$$p(Z|Y) = \frac{P(Y|Z)P(Z)}{P(Y)} \quad (7)$$

where $P(Z)$ is the prior distribution of the parameter, $P(Y|Z)$ is the probability of observing Y given Z, and $p(Z|Y)$ is the probability of the parameter Z given the observation Y. We assume that the prior probability of Θ is a Gaussian distribution with a mean of 132.1 K and a standard deviation of 2 K (ref. [26]). The prior probabilities of other parameters are uniformly distributed. Denoting the forward model as $F(Z)$ and assuming Gaussian statistics, $P(Y|Z)$ is:

$$p(Y|Z) = \frac{1}{\sqrt{(2\pi)^d|\Sigma|}}\exp\left(-\frac{1}{2}(Y - F(Z))^T \Sigma^{-1}(Y - F(Z))\right) \quad (8)$$

where $d = 15$ is the dimension of the observation vector Y, and Σ is the formal covariance matrix estimated from the deconvolution process. Σ is a block diagonal matrix with each block of size 3×3 because the five channels are independent of one another. The magnitude of the elements in Σ is illustrated by the error bars in Fig. 7. The Markov Chain Monte Carlo sampling algorithm uses 24 Markov chains with 6,000 states in each chain to fit the measurement vector.

The thermal profile is obtained by integrating the moist adiabatic temperature gradient upward to approximately 0.6 bar[40]. Then the temperature profile is replaced by the Cassini/CIRS observations in the upper troposphere and stratosphere[38]. Similarly, the compositional profiles are constant up to the condensation levels of each species, except for ammonia, which is modified slightly according to the description in the main text. Then their abundances follow their saturation vapour curves assuming 100% relative humidity and are replaced with the Cassini/CIRS observations for pressures less than 0.6 bar.

Data availability
Juno MWR data can be accessed on the Planetary Data System (PDS) https://pds. nasa.gov/. Requests for all other data or materials that are presented in the paper but not archived in the PDS should be addressed to C.L.

References
1. Weidenschilling, S. & Lewis, J. Atmospheric and cloud structures of the Jovian planets. *Icarus* **20**, 465–476 (1973).
2. Atreya, S. K. & Wong, A.-S. Coupled clouds and chemistry of the giant planets—a case for multiprobes. *Space Sci. Rev.* **116**, 121–136 (2005).
3. Lewis, J. S. & Prinn, R. G. Jupiter's clouds: structure and composition. *Science* **169**, 472–473 (1970).
4. Gierasch, P. J. Jovian meteorology: large-scale moist convection. *Icarus* **29**, 445–454 (1976).
5. Gierasch, P. J. et al. Observation of moist convection in Jupiter's atmosphere. *Nature* **403**, 628 (2000).
6. Wong, M. H. et al. Oxygen and other volatiles in the giant planets and their satellites. *Rev. Mineral. Geochem.* **68**, 219–246 (2008).
7. Young, R. E., Smith, M. A. & Sobeck, C. K. Galileo probe: in situ observations of Jupiter's atmosphere. *Science* **272**, 837–838 (1996).
8. Orton, G. S. et al. Characteristics of the Galileo probe entry site from Earth-based remote sensing observations. *J. Geophys. Res. Planets* **103**, 22791–22814 (1998).
9. Niemann, H. et al. The composition of the Jovian atmosphere as determined by the Galileo probe mass spectrometer. *J. Geophys. Res. Planets* **103**, 22831–22845 (1998).
10. Wong, M. H., Mahaffy, P. R., Atreya, S. K., Niemann, H. B. & Owen, T. C. Updated Galileo probe mass spectrometer measurements of carbon, oxygen, nitrogen, and sulfur on Jupiter. *Icarus* **171**, 153–170 (2004).
11. Showman, A. P. & Ingersoll, A. P. Interpretation of Galileo probe data and implications for Jupiter's dry downdrafts. *Icarus* **132**, 205–220 (1998).
12. Owen, T. et al. A low-temperature origin for the planetesimals that formed Jupiter. *Nature* **402**, 269 (1999).
13. Mousis, O., Lunine, J. I., Madhusudhan, N. & Johnson, T. V. Nebular water depletion as the cause of Jupiter's low oxygen abundance. *Astrophys. J. Lett.* **751**, L7 (2012).
14. Gautier, D., Hersant, F., Mousis, O. & Lunine, J. I. Enrichments in volatiles in Jupiter: a new interpretation of the Galileo measurements. *Astrophys. J.* **550**, L227–L230 (2001).
15. Owen, T. & Encrenaz, T. Element abundances and isotope ratios in the giant planets and Titan. *Space Sci. Rev.* **106**, 121–138 (2003).
16. Helled, R. & Lunine, J. Measuring Jupiter's water abundance by Juno: the link between interior and formation models. *Mon. Not. R. Astron. Soc.* **441**, 2273–2279 (2014).
17. Lunine, J. I. & Hunten, D. M. Moist convection and the abundance of water in the troposphere of Jupiter. *Icarus* **69**, 566–570 (1987).
18. Li, C. & Ingersoll, A. P. Moist convection in hydrogen atmospheres and the frequency of Saturn's giant storms. *Nat. Geosci.* **8**, 398–403 (2015).
19. Janssen, M. A. et al. MWR: microwave radiometer for the Juno mission to Jupiter. *Space Sci. Rev.* **213**, 139–185 (2017).
20. Li, C. et al. The distribution of ammonia on Jupiter from a preliminary inversion of Juno microwave radiometer data. *Geophys. Res. Lett.* **44**, 5317–5325 (2017).
21. Brown, S. et al. Prevalent lightning sferics at 600 megahertz near Jupiter's poles. *Nature* **558**, 87 (2018).
22. Bolton, S. J. et al. Jupiter's interior and deep atmosphere: the initial pole-to-pole passes with the Juno spacecraft. *Science* **356**, 821–825 (2017).
23. Achterberg, R. K., Conrath, B. J. & Gierasch, P. J. Cassini CIRS retrievals of ammonia in Jupiter's upper troposphere. *Icarus* **182**, 169–180 (2006).
24. de Pater, I., Sault, R., Butler, B., DeBoer, D. & Wong, M. H. Peering through Jupiter's clouds with radio spectral imaging. *Science* **352**, 1198–1201 (2016).
25. Li, C. & Chen, X. Simulating Nonhydrostatic Atmospheres on Planets (SNAP): formulation, validation, and application to the Jovian atmosphere. *Astrophys. J. Suppl. Ser.* **240**, 37 (2019).
26. Lindal, G. F. et al. The atmosphere of Jupiter: an analysis of the Voyager radio occultation measurements. *J. Geophys. Res. Space Phys.* **86**, 8721–8727 (1981).
27. Bellotti, A., Steffes, P. G. & Chinsomboon, G. Corrigendum to "Laboratory measurements of the 5-20 cm wavelength opacity of ammonia, water vapor, and methane under simulated conditions for the deep jovian atmosphere" [Icarus 280 (2016) 255–267]. *Icarus* **284**, 491–492 (2016).
28. Asplund, M., Grevesse, N., Sauval, A. J. & Scott, P. The chemical composition of the Sun. *Ann. Rev. Astron. Astrophys.* **47**, 481–522 (2009).
29. Atreya, S. K. et al. in *Saturn in the 21st Century* Vol. 20, 5–43 (eds Baines, K. H. et al.) (Cambridge Univ. Press, 2019).
30. Folkner, W. M., Woo, R. & Nandi, S. Ammonia abundance in Jupiter's atmosphere derived from the attenuation of the Galileo probe's radio signal. *J. Geophys. Res. Planets* **103**, 22847–22855 (1998).
31. de Pater, I. et al. Jupiter's ammonia distribution derived from VLA maps at 3–37 GHz. *Icarus* **322**, 168–191 (2019).
32. Bjoraker, G. L. et al. The gas composition and deep cloud structure of Jupiter's Great Red Spot. *Astron. J.* **156**, 101 (2018).
33. Leconte, J., Selsis, F., Hersant, F. & Guillot, T. Condensation-inhibited convection in hydrogen-rich atmospheres—stability against double-diffusive processes and thermal profiles for Jupiter, Saturn, Uranus, and Neptune. *Astron. Astrophys.* **598**, A98 (2017).
34. Friedson, A. J. & Gonzales, E. J. Inhibition of ordinary and diffusive convection in the water condensation zone of the ice giants and implications for their thermal evolution. *Icarus* **297**, 160–178 (2017).
35. Lodders, K. Jupiter formed with more tar than ice. *Astrophys. J.* **611**, 587–597 (2004).
36. Ingersoll, A. P., Kanamori, H. & Dowling, T. E. Atmospheric gravity waves from the impact of comet Shoemaker-Levy 9 with Jupiter. *Geophys. Res. Lett.* **21**, 1083–1086 (1994).
37. Allison, M. Planetary waves in Jupiter's equatorial atmosphere. *Icarus* **83**, 282–307 (1990).
38. Fletcher, L. N. et al. Retrievals of atmospheric variables on the gas giants from ground-based mid-infrared imaging. *Icarus* **200**, 154–175 (2009).
39. Goodman, J. & Weare, J. Ensemble samplers with affine invariance. *Commun. Appl. Math. Comput. Sci.* **5**, 65–80 (2010).
40. Li, C., Ingersoll, A. P. & Oyafuso, F. Moist adiabats with multiple condensing species: a new theory with application to giant-planet atmospheres. *J. Atmos. Sci.* **75**, 1063–1072 (2018).

Author contributions
C.L. developed the inversion software and performed the data analysis. All authors discussed the results and commented on the manuscript.

Competing interests
The authors declare no competing interests.

Additional information
**Extended data** is available for this paper at https://doi.org/10.1038/s41550-020-1009-3.

Supplementary information is available for this paper at https://doi.org/10.1038/s41550-020-1009-3.

Correspondence and requests for materials should be addressed to C.L.

Reprints and permissions information is available at www.nature.com/reprints.

Publisher's note Springer Nature remains neutral with regard to jurisdictional claims in published maps and institutional affiliations.
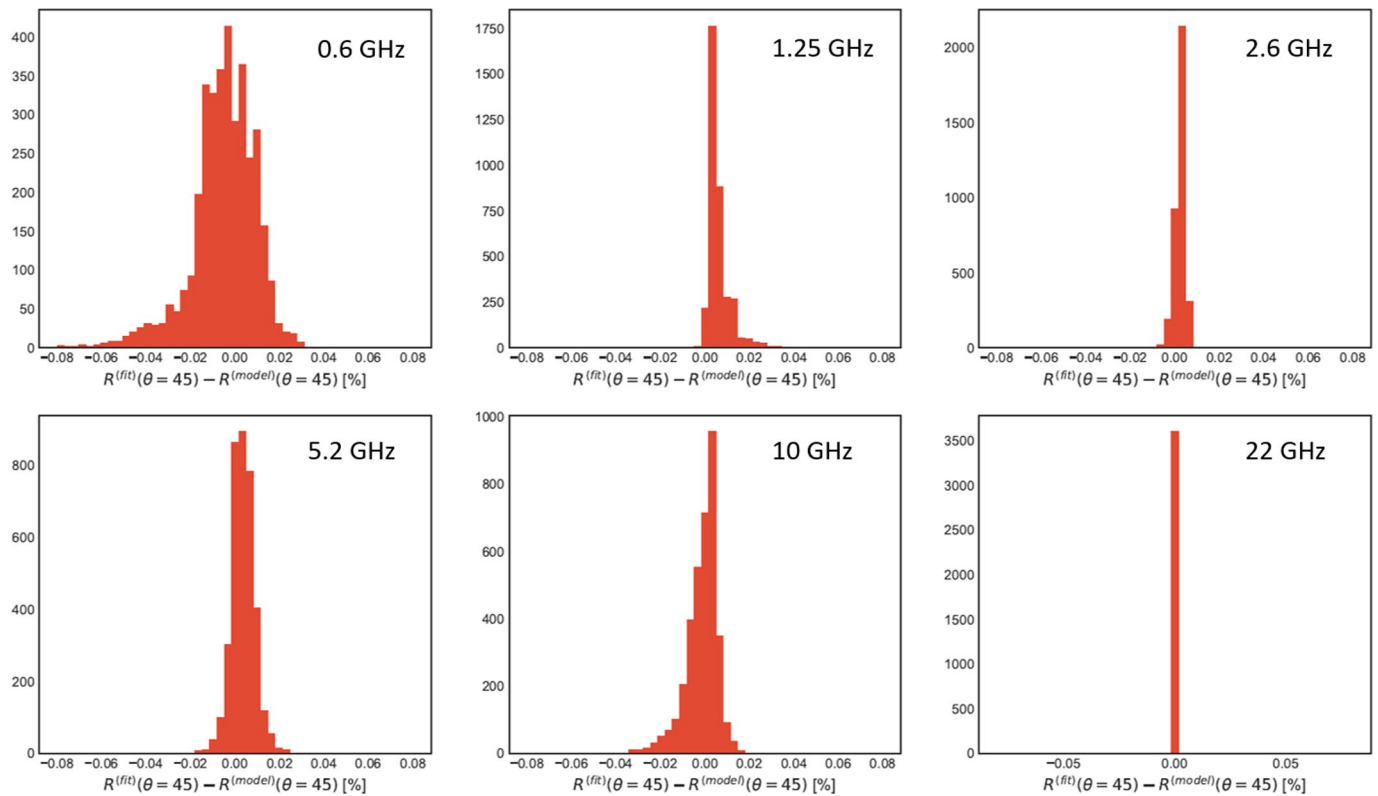
Extended Data Fig. 1 | Limb-darkening error of the fitting using a three-parameter formula. Histogram of the difference between the limb-darkening at 45° calculated using equation (4)—$R^{(fit)}$—and using a radiative transfer model— $R^{(model)}$—for a wide range of model atmospheres.
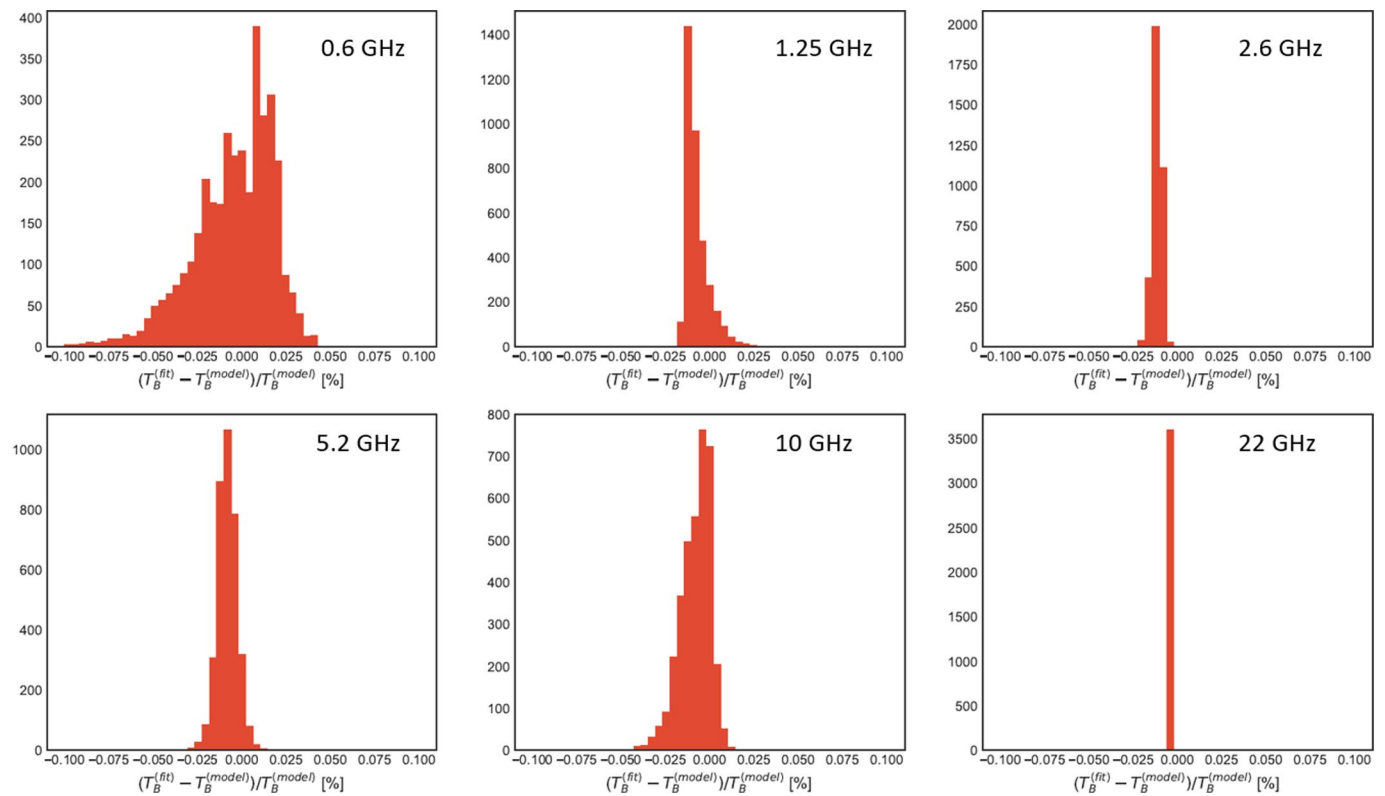
Extended Data Fig. 2 | Brightness temperature error of the fitting using a three-parameter formula. Histogram of the percentage difference between the brightness temperature calculated using equation (4)—$T_B^{(fit)}$—and using a radiative transfer model—$T_B^{(model)}$—over a wide range of model atmospheres.
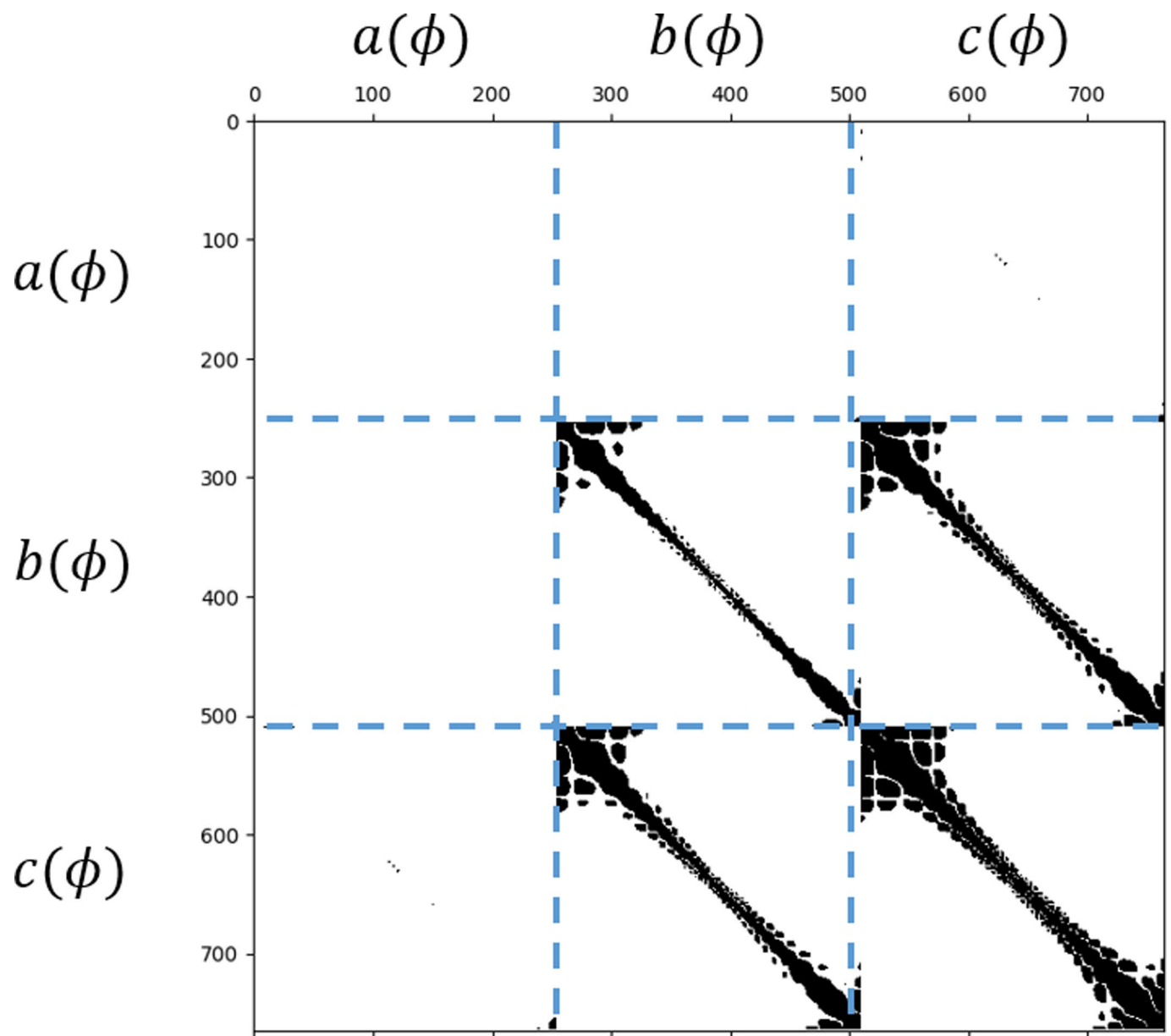
Extended Data Fig. 3 | Spacity pattern of the error covariance matrix. Sparsity pattern of the covariance matrix of X* in equation (6) (10 GHz). The coefficients are aligned sequentially from $a(\phi)$ to $b(\phi)$ to $c(\phi)$. The dark region indicates that the covariance is large.